



## Myelin and iron concentration in the human brain: A quantitative study of MRI contrast



Carsten Stüber<sup>a,\*</sup>, Markus Morawski<sup>b,c</sup>, Andreas Schäfer<sup>a</sup>, Christian Labadie<sup>a,e</sup>, Miriam Wähnert<sup>a</sup>, Christoph Leuze<sup>a</sup>, Markus Streicher<sup>a</sup>, Nirav Barapatre<sup>d</sup>, Katja Reimann<sup>a</sup>, Stefan Geyer<sup>a</sup>, Daniel Spemann<sup>d</sup>, Robert Turner<sup>a</sup>

<sup>a</sup> Department of Neurophysics, Max Planck Institute for Human Cognitive and Brain Sciences, Stephanstrasse 1a, 04103 Leipzig, Germany

<sup>b</sup> Paul-Flechsig-Institute for Brain Research, Faculty of Medicine, University of Leipzig, Jahnallee 59, 04109 Leipzig, Germany

<sup>c</sup> Department of Neuroscience and Physiology, State University of New York, Upstate Medical University, Syracuse, NY 13210, USA

<sup>d</sup> Institute of Nuclear Solid State Physics, Faculty of Physics, University of Leipzig, Linnéstrasse 5, 04103 Leipzig, Germany

<sup>e</sup> Institut Lumière et Matière, UMR5306 Université Claude Bernard Lyon I, F-69622 Villeurbanne, France

### ARTICLE INFO

#### Article history:

Accepted 25 February 2014

Available online 6 March 2014

#### Keywords:

PIXE

Phosphorus

Magnetic susceptibility

Simulations

### ABSTRACT

During the last five years ultra-high-field magnetic resonance imaging (MRI) has enabled an unprecedented view of living human brain. Brain tissue contrast in most MRI sequences is known to reflect mainly the spatial distributions of myelin and iron. These distributions have been shown to overlap significantly in many brain regions, especially in the cortex. It is of increasing interest to distinguish and identify cortical areas by their appearance in MRI, which has been shown to be feasible *in vivo*. Parcellation can benefit greatly from quantification of the independent contributions of iron and myelin to MRI contrast. Recent studies using susceptibility mapping claim to allow such a separation of the effects of myelin and iron in MRI. We show, using post-mortem human brain tissue, that this goal can be achieved. After MRI scanning of the block with appropriate  $T_1$  mapping and  $T_2^*$  weighted sequences, we section the block and apply a novel technique, proton induced X-ray emission (PIXE), to spatially map iron, phosphorus and sulfur elemental concentrations, simultaneously with  $1\ \mu\text{m}$  spatial resolution. Because most brain phosphorus is located in myelin phospholipids, a calibration step utilizing element maps of sulfur enables semi-quantitative *ex vivo* mapping of myelin concentration. Combining results for iron and myelin concentration in a linear model, we have accurately modeled MRI tissue contrasts. Conversely, iron and myelin concentrations can now be estimated from appropriate MRI measurements in post-mortem brain samples.

© 2014 Elsevier Inc. All rights reserved.

### Introduction

MR imaging at ultra-high field strength has recently provided a tremendous improvement in the *in vivo* visualization of human brain structures. This methodology now achieves  $350\ \mu\text{m}$  isotropic resolution in living human brain with feasible scan times, and can depict cortical layers consistent with known myeloarchitecture. Due to its magnetic properties and high concentration in human brain compared with

other trace metals, iron is also considered to play a significant role in MRI tissue contrast. The origins of MRI contrast in human brain have thus become once again a topic of great interest, with iron and myelin as major front-runners.

Myelin itself includes at least 340 different proteins (Jahn et al., 2009), which comprise 30% of the dry weight. The remaining 70% is comprised of lipids: cholesterol (20%), galactolipids (20%) and phospholipids (30%) of total dry weight (Norton and Autilio, 1966). Specific components of myelin have been shown to play a disproportionate role in MR spin relaxation (Kucharczyk et al., 1994).

Early studies showed a reasonably good correspondence between MR image intensity within the cortex and known histological myeloarchitecture (Clark et al., 1991; Eickhoff et al., 2005; Fatterpekar et al., 2002; Walters et al., 2007). Laule et al. (2008) investigated the relationship between MRI signal and myelin, in the context of MR measurement of the myelin water fraction (MWF) in the brains of multiple sclerosis patients, using myelin-stained cadaver brain sections. Analogously, standard histological staining procedures have been used for exploring the distribution of iron in human brain tissue, employing Perls'

\* Corresponding author.

E-mail addresses: [stueber@cbs.mpg.de](mailto:stueber@cbs.mpg.de) (C. Stüber),

[Markus.Morawski@medizin.uni-leipzig.de](mailto:Markus.Morawski@medizin.uni-leipzig.de) (M. Morawski), [schaefer@cbs.mpg.de](mailto:schaefer@cbs.mpg.de) (A. Schäfer), [labadie@cbs.mpg.de](mailto:labadie@cbs.mpg.de) (C. Labadie), [wahnert@cbs.mpg.de](mailto:wahnert@cbs.mpg.de) (M. Wähnert), [leuze@cbs.mpg.de](mailto:leuze@cbs.mpg.de) (C. Leuze), [streicher@cbs.mpg.de](mailto:streicher@cbs.mpg.de) (M. Streicher), [barapatre@physik.uni-leipzig.de](mailto:barapatre@physik.uni-leipzig.de) (N. Barapatre), [reimann@cbs.mpg.de](mailto:reimann@cbs.mpg.de) (K. Reimann), [sgeyer@cbs.mpg.de](mailto:sgeyer@cbs.mpg.de) (S. Geyer), [spemann@uni-leipzig.de](mailto:spemann@uni-leipzig.de) (D. Spemann), [turner@cbs.mpg.de](mailto:turner@cbs.mpg.de) (R. Turner).

Prussian blue for trivalent iron and Turnbull's blue for divalent iron (Drayer et al., 1986). However, these histological techniques are known to be unreliable. Some iron is masked and therefore not stained in the brain tissue, giving a biased presentation of the true content of this element. Similarly, the quality of myelin staining varies considerably, depending on the type of fixation used, the post-mortem delay before fixation, the temperature of the stain bath, and the precise type of stain used.

The optical density of stained histological sections provides information that a particular substance is present at a particular location. Nevertheless, the densities of any tissue component cannot be absolutely quantified.

To circumvent these limitations, we introduce a state-of-the-art technique, the so-called proton-induced X-ray emission (PIXE) (Butz et al., 2005). Here a tightly focused ion beam of high energetic protons is used to analyze a very thin slice of brain tissue (Morawski et al., 2005). These ions collide with atoms within the tissue, allowing spatially resolved quantification of elements, irrespective of their chemical state, with a resolution down to 1  $\mu\text{m}$ . The collisions produce X-rays with an energy spectrum highly specific to each chemical element, allowing quantitative determination of the spatial distribution of elements within the sample, and in particular demonstrating the elemental distribution of iron within brain gray and white matter. It should be pointed out that because the proton beam is negligibly attenuated as it passes through the very thin tissue slice, the atoms of a given element are equally mapped; there are no shadowing effects.

A novel insight regarding this technique arises from considering the elementary maps of phosphorus available using the PIXE technique. Phosphorus is present in proteins in the form of phosphomonoester and phosphodiester, found in the helical strands of the DNA. Furthermore phosphorus is found in phosphocreatine and nucleoside phosphates such as ATP and ADP, which are essential for intracellular energy storage and transfer. However, the main portion of phosphorus is located in phospholipids, accounting for around 80% of all phosphorus in white matter and 60% in gray matter (Buchli et al., 1994). This suggests that the chemical element phosphorus might be used to assess the myelin concentration quantitatively, in contrast with histological staining approaches. Additionally, the element sulfur is present in sulfatides, which together with cerebroside forms the group of galactolipids, highly abundant in myelin. Hence sulfur can be additionally used as a marker for myelin distribution in brain tissue.

In this study, we use PIXE methodology to assess the contribution of iron and myelin as sources of MRI contrast in commonly used sequences: MP2RAGE, yielding  $T_1$  maps, and FLASH, yielding  $T_2^*$  weighted images and quantitative susceptibility maps (QSMs) (Reichenbach, 2012). Furthermore, we investigate the distribution of iron in human brain tissue. Early work on iron concentration in white and cortical gray matter by Hallgren and Sourander (1958) suggested a similar distribution in both regions, contradicted by later findings by Drayer et al. (1986) and Fukunaga et al. (2010). Recent studies by Duyn et al. (2007) show strong phase differences in the cortex and white matter, which cannot easily be explained by the small differences in iron content claimed in earlier works. Modern QSM quantitative techniques allow testing of the validity of theoretical physical models which have attempted to derive regression coefficients for the relative contributions of iron and myelin in  $T_1$  maps (Rooney et al., 2007),  $T_2^*$  maps and QSM (Schweser et al., 2011).

## $T_1$

Several publications have indicated a relationship between the longitudinal relaxation rate  $R_1$  ( $R_1 = 1/T_1$ ) and myelin content. The conclusions of those studies are typically vague statements such as “ $T_1$  reflects myeloarchitecture” (Geyer et al., 2011) or “there is a strong relationship between  $R_1$  and tissue myelin content” (Sigalovsky et al., 2006). Glasser and van Essen (2011) assert without much experimental justification that myelin can be mapped by taking the ratio

between  $T_1$  weighted and ‘ $T_2$  weighted’ images. There have been only a few quantitative attempts to find a relationship between myelin content and  $T_1$  (Bot et al., 2004; Mottershead et al., 2003; Schmierer et al., 2004), which has been reviewed recently by Laule et al. (2007). Conventional imaging techniques are not capable of directly measuring the myelin concentration, so that such relationships were indirectly determined. Additionally it is unclear how much iron content contributes to  $T_1$  tissue contrast (Gelman et al., 2001). Since iron and myelin often colocalize within the cortex (Fukunaga et al., 2010), it cannot be excluded that cortical  $T_1$  contrast is partly caused by iron, in particular ferritin molecules (Gossuin et al., 2000), and not exclusively by myelin lipids, in which cholesterol is highly abundant (Koenig, 1991). The literature regarding iron and  $T_1$  contrast is controversial: data showing a clear relationship between brain  $T_1$  and iron concentration (Ogg and Steen, 1998; Vymazal et al., 1995) contradict other publications showing no significant correlation of  $T_1$  and iron (Steen et al., 2000). Rooney et al. (2007) showed further evidence of a role of iron in  $T_1$  contrast in regions of the thalamus (low iron content) and the globus pallidus (high iron content), besides significant contributions from ‘macromolecules’. Rooney and coworkers hypothesize that  $R_1$  is a linear function of iron and ‘macromolecule’ concentration in the form:

$$R_1 = a_{\text{Fe}}c_{\text{Fe}} + a_{\text{M}}c_{\text{M}} + a_{\text{off}}, \quad (1)$$

where  $c_{\text{Fe}}$  is the iron concentration,  $c_{\text{M}}$  is the macromolecular concentration expressed in volume fraction,  $a_{\text{off}}$  the relaxivity of a pure saline solution and  $a_{\text{M}}$  and  $a_{\text{Fe}}$  are the relaxivities of iron and macromolecular sites, respectively.<sup>1</sup> From this study the authors infer a dominant role for ‘macromolecules’ and a lesser contribution from iron. Rooney et al. do not differentiate the origin of the macromolecular content, whereas Koenig et al. (1990) suggest a direct involvement of the hydroxyl of cholesterol, located 0.5 nm below the headgroups of the phospholipids and galactolipids of the myelin membrane (see Fig. 6A in O’Brien (1965)). Recently, a multi-exponential study of longitudinal relaxation in white matter revealed a rapidly relaxing water  $T_1$  component attributed to myelin water (Labadie et al., 2014). The observed myelin water fraction was correlated to the  $T_1$  of the slower relaxing component, giving additional evidence of a role of myelin in the shortening of the apparent  $T_1$  observed by conventional mono-exponential measurements.

## $T_2^*/\text{QSM}$

$T_2^*$  relaxation (and its inverse,  $R_2^* = 1/T_2^*$ ) describes the loss of transverse magnetization caused by spin–spin relaxation, as well as by progressive phase incoherence associated with magnetic field inhomogeneities (Chavhan et al., 2009). Water in close proximity to paramagnetic iron experiences local magnetic field gradients, thus appearing hypointense on  $T_2$  weighted MR images (Ordidge et al., 1994), notably in regions with high iron deposits (Drayer et al., 1986). Because it is of clinical interest to visualize brain iron, for instance in Parkinson’ disease, much recent research has focused on the relationship between iron and  $R_2^*$  (Langkammer et al., 2011; Ordidge et al., 1994; Yan et al., 2012). Schenck and Zimmerman (2004) already proposed to use  $T_2^*$  weighted high-field magnetic resonance imaging as a biomarker for mapping brain iron. Recently the main focus has shifted to susceptibility weighted imaging (Duyn, 2010; Li et al., 2011; Yao et al., 2009) and thence to quantitative susceptibility mapping (QSM), which is better able to visualize the iron distribution in brain tissue (Langkammer et al., 2012; Schäfer et al., 2012). While noting the importance of iron in  $T_2^*$  decay and susceptibility mapping, other experimenters have tried to explain the heterogeneity of MR image intensity found in

<sup>1</sup> In this work, the constant  $a_{\text{M}}$  and the macromolecular concentration  $c_{\text{M}}$  are replaced by  $a_{\text{My}}$  and  $c_{\text{My}}$  respectively to only take the myelin content into account.

human brain white matter by appeal to differences in myelin concentration (Li et al., 2009). Not only tissue composition has been considered, but also the orientation of myelinated fibers within white matter appears to play a role in  $R_2^*$  variations (Bender and Klose, 2010; Li et al., 2009). Similar to  $R_1$ , linear models have been proposed to describe the tissue contrast of myelin and iron in brain tissue:

$$R_2^*(c_{Fe}, c_{My}) = b_{Fe} * c_{Fe} + b_{My} * c_{My} + b_{Off} \quad (2)$$

$$\chi(c_{Fe}, c_{My}) = d_{Fe} * c_{Fe} + d_{My} * c_{My} + d_{Off}, \quad (3)$$

where  $R_2^*$  is the effective transverse relaxation rate,  $\chi$  the voxel bulk magnetic susceptibility,  $c_{Fe}$  and  $c_{My}$  are the storage iron and myelin concentration respectively and  $b_{Fe}$ ,  $b_{My}$ ,  $b_{Off}$ ,  $d_{Fe}$ ,  $d_{My}$  and  $d_{Off}$  are the coefficients (Schweser et al., 2011).

To approach the task of correlating MR image intensity with iron and myelin concentrations, we studied two easily identifiable cortical areas in the human brain, possessing different characteristic features: the primary visual cortex (V1), containing the stria of Gennari (SoG) and the central sulcus, which contains the boundary between the primary motor- and primary somatosensory cortices (M1/S1). The SoG, a band of Baillarger visible to the naked eye, is a 300  $\mu$ m thick myelinated layer within the primary visual cortex (Barbier et al., 2002; Clark et al., 1991; Trampel et al., 2011).

The motor cortex, as compared with the somatosensory cortex, is thicker and has a different laminar structure, and thus provides a useful example for comparisons of cortical iron content.

Furthermore for testing the validity of determining MR maps as a combination of iron and myelin concentration we inversely calculated iron and myelin maps from MR maps and compared these maps with measured PIXE maps. For this purpose we chose a region remote from the cortex, the subthalamic nucleus, a deep gray matter nucleus of the basal ganglia system, known to contain iron and myelin.

## Methods

### Brain samples

Two human post-mortem brains (male, 62 years, postmortem time before fixation 36 h; female, 70 years, post-mortem time before fixation 28 h) were obtained from the Neuropathology Department of the University of Leipzig, Leipzig, Germany. One other fixed, excised brain block of the precentral/postcentral gyrus (female, 85 years, post-mortem time before fixation 8 h) was obtained, with informed consent from the donor, from the Netherlands Brain Bank, Amsterdam, Netherlands. The brain blocks were fixed in 4% formaldehyde for 30 days prior to MR scanning and the subsequent histological processing.

### MRI scanning

Portions of the posterior occipital lobe, pre-/postcentral gyrus and subthalamic nucleus were resected from the donated human brains into blocks of a similar size to the block supplied by the Netherlands Brain Bank. All blocks were positioned within acrylic spheres of 6 cm diameter, immersed in Fomblin (Solvay Solexis, Bollate, Italy) to eliminate background MRI signal, and scanned with a 7 T MR scanner (MAGNETOM 7 T, Siemens Healthcare Sector, Erlangen, Germany) equipped with a special homebuilt square single or dual-channel RF coil (120 mm) to increase signal to noise ratio. The MP2RAGE sequence (Marques et al., 2010), which utilizes two different echo times, was used to acquire  $T_1$  maps (repetition time  $TR = 3$  s, echo time  $TE = 3.17$  ms, inversion times  $TI_1 = 300$  ms,  $TI_2 = 900$  ms, 0.2 mm or 0.1 mm isotropic). FLASH sequences were used to acquire gradient echo (GRE)  $T_2^*$  weighted images. Both magnitude and phase images were reconstructed and stored. GRE images with a single echo time were acquired

within a period of 42 h to provide images with 70  $\mu$ m isotropic resolution ( $TR = 50$  ms,  $TE = 11.1$  ms). GRE images with eight echo times were also acquired ( $TE_1 = 3.26$  ms,  $TE_2 = 9.35$  ms,  $TE_3 = 15.44$  ms,  $TE_4 = 21.53$  ms,  $TE_5 = 27.62$  ms,  $TE_6 = 33.71$  ms,  $TE_7 = 39.8$  ms,  $TE_8 = 45.89$  ms), to allow calculation of  $T_2^*$  maps with 200  $\mu$ m isotropic resolution.

### Histology

The fixed and 30% sucrose cryoprotected blocks were frozen (Zeiss Hyrax KS 34, Jena, Germany), and sliced with a microtome (Leica SM 2000 R, Wetzlar, Germany) into 30  $\mu$ m thick sections in the same orientation as the MR image acquisition. Successive sections were stained with standard histochemical and immunohistochemical (IHC) procedures for myelin basic protein (MBP) (IHC, myelin stain), SMI-311 (IHC, cell stain), Perls' iron stain (histochemical iron stain), CRTL-1 stain (IHC, extracellular matrix stain) and Sudan black B (histochemical lipid stain). Adjacent sections were kept unstained for PIXE measurements. The unstained sections were embedded in mounting medium (DePeX®, Merck, Darmstadt, Germany), a mixture of polystyrene ( $C_8H_8$ ) and the plasticizer di-butylphthalate ( $C_{16}H_{22}O_4$ ) with an assumed ratio between carbon and hydrogen of approximately 1:1 ( $C_{10}H_{10}$ ) and mounted on a frame for subsequent measurements.

### Removal of iron

Two excised blocks (visual cortex; motor-/somatosensory cortex) were soaked in a solution of 2% deferoxamine and 2% sodium dithionite for a period of 15 days to virtually completely extract the iron. After this treatment the two blocks were scanned again with exactly the same parameters as used previous to this treatment.

### PIXE scanning

The unstained, embedded sections were measured at the Leipzig ion beam laboratory (LIPSION, University of Leipzig, Leipzig, Germany) (Reinert et al., 2011). A proton beam of 2.25 MeV, 1–2 nA and a diameter of about 1  $\mu$ m was used for all experiments to scan the samples line-by-line. The charged particles strike the sample, mounted in a vacuum chamber, and knock out the inner shell electrons of the atoms. The inner orbits are subsequently filled with outer electrons, which emit element-specific, so-called characteristic X-rays during transition. This mapping technique thus allows an element-specific investigation of the sample. The so-called particle (or proton) induced X-ray emission (PIXE) was used to spatially resolve the distribution and concentration of iron, phosphorus and sulfur. Besides the X-ray signal, Rutherford backscattering spectrometry (RBS) was used to obtain simultaneous information on the matrix composition (C, N, O directly and H indirectly), accumulated beam charge and sample thickness, using the RUMP code (Doolittle, 1985) for BS-spectrum fitting.

Each large single scan takes 90 min. and covers a field of view (FOV) of  $3.2 \times 3.2$  mm<sup>2</sup> with  $1000 \times 1000$  pixels, which corresponds to a spatial resolution of about (3  $\mu$ m)<sup>2</sup>. Analogously a small single scan takes 23 min and covers a FOV of  $1.6 \times 1.6$  mm<sup>2</sup> with  $500 \times 500$  pixels. The quantitative analysis of the matrix composition was performed using the PIXE data analysis program GeoPIXE II (Ryan, 2001). The single measurements, consisting of 8–16 small or large FOVs and a complete measurement time of 12–16 h were assembled as a mosaic. Matlab code was used to adjust for small differences of the applied charge within each measurement (Matlab 7.0, Mathworks, Natick, USA).

### Myelin maps

Myelin maps were estimated using phosphorus maps ( $n_{All}^P$ ), with the aid of sulfur maps ( $n_{All}^S$ ).



To enable this estimation, a number of assumptions were required. These are as follows:

- (i) Within unmyelinated brain tissue, averaged over a distance scale of 100  $\mu\text{m}$ , the ratio between the local atomic densities of phosphorus and sulfur is assumed to be spatially constant.
- (ii) The molecular composition of myelin is assumed to be spatially uniform, so that the ratio between the atomic densities of sulfur and phosphorus in myelin is spatially constant.
- (iii) The difference between gray and white matter in the atomic compositions of phosphorus and sulfur can be accounted for entirely by the presence of myelin in white matter (Norton and Cammer, 1984).
- (iv) Excluding myelin, the atomic concentrations of phosphorus and sulfur are assumed to be identical in gray and white matter. This is a plausible assumption given that this remaining tissue comprises cytoplasm, cell organelles and nuclei both in gray and in white matter.
- (v) Stable, compact myelin is assumed to contain no protein-associated phosphorus, but only phospholipids.
- (vi) The preparation of tissue samples for PIXE scanning washes out all small mobile phosphorus-containing molecules such as ATP and ADP.
- (vii) White matter contains an average of 50% myelin by dry weight (Norton and Cammer, 1984).

The phosphorus and sulfur atomic concentration maps each contain a fraction that is associated with myelin ( $n_{\text{My}}^{\text{P}}$ ,  $n_{\text{My}}^{\text{S}}$ ) and a fraction associated with the remaining tissue, including cells, axons, etc. ( $n_{\text{Rest}}^{\text{P}}$ ,  $n_{\text{Rest}}^{\text{S}}$ ). Thus  $n_{\text{All}}^{\text{P}}$  and  $n_{\text{All}}^{\text{S}}$  can be written in the following form:

$$n_{\text{All}}^{\text{P}} = n_{\text{My}}^{\text{P}}(x, y) + n_{\text{Rest}}^{\text{P}}(x, y) = f_{\text{My}}^{\text{P}} \cdot c_{\text{My}}(x, y) + f_{\text{Rest}}^{\text{P}} \cdot c_{\text{Rest}}(x, y) \quad (4)$$

$$n_{\text{All}}^{\text{S}} = n_{\text{My}}^{\text{S}}(x, y) + n_{\text{Rest}}^{\text{S}}(x, y) = f_{\text{My}}^{\text{S}} \cdot c_{\text{My}}(x, y) + f_{\text{Rest}}^{\text{S}} \cdot c_{\text{Rest}}(x, y), \quad (5)$$

where  $c_{\text{My}}$  and  $c_{\text{Rest}}$  are the concentrations of myelin and the rest of the tissue, respectively. The coefficients  $f_{\text{My}}^{\text{P}}$  and  $f_{\text{My}}^{\text{S}}$  denote the fractions of phosphorus and sulfur in myelin. Similarly,  $f_{\text{Rest}}^{\text{P}}$  and  $f_{\text{Rest}}^{\text{S}}$  denote the fractions of phosphorus and sulfur contained in the rest of the tissue, which is assumed to be fairly homogeneous across the brain (assumption (iv)).

For the determination of phosphorus that is associated with myelin ( $n_{\text{My}}^{\text{P}}$ ), we assume (i) that in unmyelinated brain tissue there is a constant ratio between phosphorus and sulfur density on the macroscopic scale, associated with proteins and other large non-lipid biological molecules such as DNA. This ratio can be determined in cortical layer II, which is known to be free of myelin almost everywhere in the brain. The corresponding measurement was made, giving

$$k_{\text{Rest}} = n_{\text{Rest}}^{\text{P}}(x, y) / n_{\text{Rest}}^{\text{S}}(x, y) = f_{\text{Rest}}^{\text{P}} / f_{\text{Rest}}^{\text{S}} = 0.32 \pm 0.15. \quad (6)$$

The phosphorus and sulfur levels in this layer can thus be used as a calibration standard to determine the constant  $k_{\text{Rest}}$ . Ten profiles in neighboring regions were taken to determine  $k_{\text{Rest}}$ . Furthermore we assume (ii) that the ratio of sulfur and phosphorus in myelin is constant:

$$k_{\text{My}} = n_{\text{My}}^{\text{P}}(x, y) / n_{\text{My}}^{\text{S}}(x, y) = f_{\text{My}}^{\text{P}} / f_{\text{My}}^{\text{S}} = 3.1 \pm 0.2. \quad (7)$$

This constant  $k_{\text{My}}$  was determined using data at the white/gray matter boundary from 10 profiles. It can be assumed (iii) that the difference between gray and white matter is myelin (Norton and Cammer, 1984). If the crucial assumptions (i) and (iv) are also correct, this implies that the difference of phosphorus concentrations in gray and in white

matter divided by the difference of sulfur concentrations in gray and in white matter is  $k_{\text{My}}$ :

$$k_{\text{My}} = \frac{f_{\text{My}}^{\text{P}} (c_{\text{My}}(\text{WM}) - c_{\text{My}}(\text{GM})) + f_{\text{Rest}}^{\text{P}} (c_{\text{Rest}}(\text{WM}) - c_{\text{Rest}}(\text{GM}))}{f_{\text{My}}^{\text{S}} (c_{\text{My}}(\text{WM}) - c_{\text{My}}(\text{GM})) + f_{\text{Rest}}^{\text{S}} (c_{\text{Rest}}(\text{WM}) - c_{\text{Rest}}(\text{GM}))} = \frac{f_{\text{My}}^{\text{P}}}{f_{\text{My}}^{\text{S}}}. \quad (8)$$

The experimental measurement ( $k_{\text{My}} = 3.1 \pm 0.2$ ) was verified by theoretical calculation ( $k_{\text{My}} = 3.24$ ). The theoretical value was calculated in the following way: Jahn et al. (2009) showed that the fraction of Proteolipid protein (PLP) and Myelin basic protein (MBP) is enriched in compact myelin, thus it is assumed that both proteins 'represent' compact myelin (ratio PLP/MBP = 17:8). PLP contains 14 cysteine residues: 4 involved in disulfide bridges (residue numbers: 183, 200, 219, 227), 4 in transmembrane helices (24, 32, 34, 168) and 6 thioester-linked fatty acids (5, 6, 9, 109, 138, 140) and furthermore 4 methionine residues (205, 234, 257, 270) (Ng and Deber, 2010). Thus, one PLP contains 18 sulfur atoms. MBP contains two units of methionine (21, 185), corresponding to 2 sulfur atoms (Harauz et al., 2004).

O'Brien and Sampson (1965) assumed a molecular weight of 28 kDa for myelin proteins and calculated that for each protein molecule in human myelin there are 186 lipid molecules in the following ratio: cholesterol (75); phosphatidyl ethanolamine (25); serine glycerophosphatide (9); choline glycerophosphatide (20); sphingomyelin (9); cerebroside (29); cerebroside sulfate (7); ceramide (3); and uncharacterised lipids (9). The headgroup of a phospholipid contains one phosphorus element, and that of a sulfatide one sulfur element, thus for each protein there are 63 phosphorus atoms ( $25 + 9 + 20 + 9$ ) and 7 sulfur atoms associated with lipids. However, the molecular weight of 28 kDa for proteins was an estimation, Jahn et al., 2009 takes a value of 29.9 kDa for PLP and 18.5 kDa for MBP. Comparing both values, one needs to calculate  $18 \cdot 28 / 29.9 \cdot 17 / (17 + 8) + 2 \cdot 28 / 18.5 \cdot 8 / (17 + 8) = 12.43$ . Thus, for 7 sulfur units associated with lipids there are 12.43 sulfur units associated with proteins. In myelin there are 19.43 sulfur units and  $25 + 9 + 20 + 9 = 63$  phosphorus units, resulting in a phosphorus–sulfur ratio of 3.24, i.e. the theoretical value of  $k_{\text{My}} = 3.24$ .

This number, however, is a lower bound, since we do not consider phosphorus associated with proteins. Several units get phosphorylated during conformation change (MBP: 7, 12, 17, 19, 20, 56, 69, 71, 98, 102, 115, 136, 149, 151, 161, 163, 165), comprising 17 residues (Harauz et al., 2004), but it can be assumed (v) that compact myelin is in a stable configuration, and thus contains no protein-associated phosphorus.

Using Eqs. (4)–(7), a myelin concentration map based on the distribution of the myelin-associated phosphorus in gray and white matter can then be calculated in the following way:

$$c_{\text{My}}(x, y) \cong n_{\text{My}}^{\text{P}}(x, y) = (n_{\text{All}}^{\text{P}}(x, y) - k_{\text{Rest}} \cdot n_{\text{All}}^{\text{S}}(x, y)) / (1 - k_{\text{Rest}} / k_{\text{My}}). \quad (9)$$

This expresses a linear relationship between the concentration of myelin and the concentrations of phosphorus and sulfur in the tissue. Here the lipid composition of myelin is regarded as essentially uniform, and all mobile phosphorus-containing molecules (such as ADP and ATP) are assumed (vi) to be washed out during the fixation process.

Finally, we can infer a myelin volume fraction map from the myelin concentration map. This map of  $n_{\text{My}}^{\text{P}}$  was converted into a myelin volume fraction (MVF) map, assuming (vii) an average myelin dry weight proportion of 50% in white matter (Norton and Cammer, 1984). Assuming that the peak value of the Gaussian-shaped histogram of the myelin concentration corresponds to the average concentration of myelin, an MVF of 0.5 can be assigned to the position of the peak of the histogram. A myelin concentration  $c_{\text{My}}(x, y) = 0$  corresponds to  $\text{MVF} = 0$  and  $c_{\text{My}}(x, y) = 2 \cdot \text{peak}$  to  $\text{MVF} = 1$ .

## Magnetic susceptibility maps

The susceptibility maps were calculated using the GRE phase maps. The data were processed using a 3D phase unwrapping algorithm (Abdul-Rahman et al., 2007) and converted to ppm by dividing the unwrapped phase images by  $\gamma \times TE \times B_0$  (where  $\gamma$  is the gyromagnetic ratio,  $TE$  the echo time and  $B_0 = 7$  T the magnetic field strength). To remove large scale effects caused by  $B_0$  inhomogeneities, the unwrapped phase data were high-pass filtered using a 3rd or 4th order polynomial fit. The QSMs were created using filtered phase data and were divided by a threshold 3D dipole kernel in the Fourier domain (Wharton et al., 2010).

The histology data was used for comparison and identifying boundaries of white and gray matter.

## Image processing and analysis

Both MR and PIXE data were coregistered in MIPAV software using thin plate spline deformation (NIH, Bethesda, USA) based on identifiable landmarks (Bookstein, 1989). The landmarks were selected at salient locations, such as tissue boundaries, gray/white matter boundaries, as well as cortical layers, if visible in both image types. In this process, the PIXE maps were down-sampled to match the resolution of the MRI data. The data were then imported into Matlab format for further analysis.

Univariate linear regression analysis was used to determine the correlation between MR image intensity and maps of iron and myelin. Assuming that our MRI-derived values of  $R_1$ ,  $R_2^*$  and magnetic susceptibility  $\chi$  can be represented as linear combinations of iron and myelin concentration, as proposed previously (Rooney et al., 2007; Schweser et al., 2011), we applied multiple linear regression to find the coefficients for  $R_1$ ,  $R_2^*$  and QSM ( $\chi$ ). If the coregistered images have a size of  $n \times m$  pixel, we have  $n \times m$  equations that have to be solved. The least squares fit for this overdetermined system of linear equations, which lacks a unique solution, is obtained by applying the Moore–Penrose pseudoinverse methodology.

The inverse process of calculating iron and myelin maps from MR maps can simply be done by solving two of the three linear Eqs. (1), (2), and (3) for iron and myelin concentration,  $c_{Fe}$  and  $c_{My}$ , respectively, for example using  $R_1$  and  $R_2^*$

$$c_{Fe}(x, y) = \frac{(R_1(x, y)b_{My} - R_2^*(x, y)a_{My} - (a_{off}b_{My} - a_{My}b_{off}))}{(a_{Fe}b_{My} - a_{My}b_{Fe})} \quad (10)$$

$$c_{My}(x, y) = \frac{(R_1(x, y)b_{Fe} - R_2^*(x, y)a_{Fe} - (a_{off}b_{Fe} - a_{Fe}b_{off}))}{(a_{My}b_{Fe} - a_{Fe}b_{My})} \quad (11)$$

where  $a_{Fe}$  and  $b_{Fe}$  denote the coefficients of  $R_1$  resp.  $R_2^*$  associated with iron. Analogously,  $a_{My}$  and  $b_{My}$  denote the coefficients associated with myelin and  $a_{off}$  and  $b_{off}$  the offsets of  $R_1$  and  $R_2^*$  respectively.

SPSS was used for error calculation for single and multiple linear regressions. The standard error of the regression coefficients was calculated.

## Results

The iron and myelin distributions within human brain tissue were investigated in cortical gray and white matter of different brains using ion beam analysis, as described. These data, together with immunohistochemical and histological information and MR measurements of human brain tissue prior to sectioning were used to evaluate the contributions of iron and myelin as sources of MR tissue contrast. Figs. 1 and 2 show the good correspondence of iron, myelin and MRI contrast in different sequences. It is strikingly evident that the iron and myelin

distributions overlap considerably in cortical gray matter in the visual cortex and in motor/somatosensory cortex. In white matter, the relationship between iron and myelin content is quite different.

### Motor/somatosensory cortex (M1/S1)

Three features of iron distribution within post-mortem human brains are clearly visible. The iron map reveals a laminar structure in gray matter (average iron concentration:  $276 \pm 50$  ppm dry weight (dw)), which closely overlaps the myelinated bands of Baillarger ( $c_{Fe} = 365 \pm 40$  ppm dw) within both the motor and somatosensory cortices (Fig. 1D). Interestingly, a narrow iron-rich band is visible ( $372 \pm 30$  ppm iron dw), lying in the white matter close to the border with the cortex, which might be attributable to the presence of U-fibers. Lastly, the iron map appears patchy within white matter, in both pre- and postcentral gyri. The Perl's iron stain (Fig. 1B) shows a similar distribution as the PIXE iron map, but with a more blurred appearance. The cell stain allows precise separation of gray and white matter and also reveals cortical lamination, as expected.

### Visual cortex (V1)

It is clear that the stria of Gennari, known to be heavily myelinated, is also rich in iron (Fig. 2D), averaging  $240 \pm 30$   $\mu$ g iron per gram tissue in dry weight (corresponding to 48 ppm wet weight). CRTL-1 is a cartilage link protein and a vital part of the perineuronal nets, a form of neuronal extracellular matrix found in the cortex that has been associated with high iron concentrations. Thus the CRTL-1 stained sections show a good overlap with the cortical iron distribution (Fig. 2B). It is notable that the white matter shows a low iron concentration ( $74 \pm 20$  ppm dry weight (dw)) when compared to laminar gray matter ( $130 \pm 20$  ppm layer I–III;  $180 \pm 25$  ppm layer V, VI). Furthermore the lipid stain indicates differences of myelin content within white matter (Fig. 2A).

### $T_1/R_1$

The  $T_1$  maps show structure within the cortex as well as in white matter (Figs. 1E and 2E). Values of  $T_1$  in white matter appear to reflect mostly myelin concentration, with decreases in  $T_1$  correlating with increased myelin content, as also seen in the myelin basic protein (MBP) stain and lipid stain histological sections (Figs. 1A and 2A). The relative homogeneity of  $T_1$  in white matter is in striking agreement with the phosphorus map indicating myelin concentration (Figs. 1C and 2C).

### $T_2^*/R_2^*$

The cortical laminar structure seen in  $T_2^*$  weighted images (Figs. 1F and 2F) correlates very well with the iron maps (Figs. 1D and 2D). The white matter patchiness seen in the iron map is also visible in the  $T_2^*$  weighted image of M1/S1 (Fig. 1D), providing evidence that iron plays a role in white matter tissue contrast.

### Quantitative susceptibility maps (QSMs)

Cortical laminar structure is clearly visible in the quantitative susceptibility maps, showing bright layers in the cortex indicating paramagnetic iron (Figs. 4 and S1). Increased intracortical iron concentrations are also seen in the quantitative iron map (Fig. 3F). Contrast differences appear within diamagnetic white matter (WM) of the motor-/somatosensory area, also showing a dark rim which might corresponds to U-fibers (Fig. 1D). Furthermore, the cortical thickness appears to be greater in QSM, as compared with the magnitude image, with its boundary corresponding to this iron-rich rim in WM at the GM/WM boundary. QSM also shows patchy white matter structures, but with reversed contrast (bright spots indicating paramagnetic

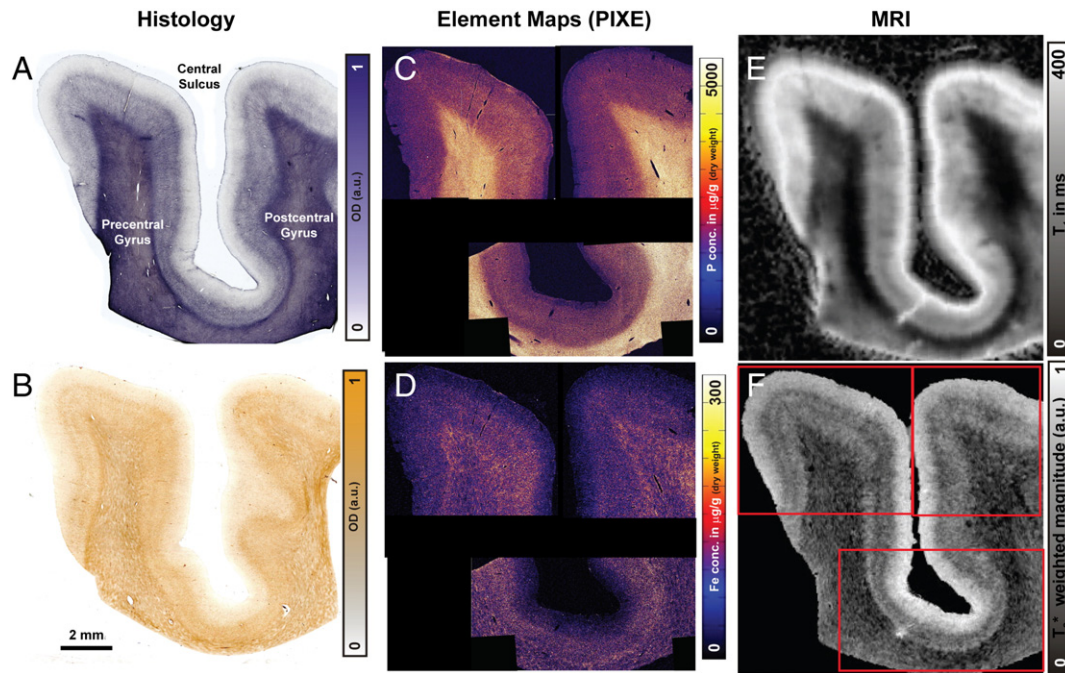


**Fig. 1.** Primary motor-/primary somatosensory cortex (M1/S1). The precentral gyrus contains the motor cortex and the postcentral gyrus contains the somatosensory cortex. (A–B) Histology. (A) Myelin basic protein stain (immunohistochemistry). (B) Perl's iron stain. (C–D) PIXE-measurements. (C) Phosphorus map. (D) Iron map. (E–F) MRI. (E)  $T_1$  map. (F)  $T_2^*$  weighted image.

substances), similar to the non-uniformity within white matter of the iron map.

#### Determination of contrast contribution

Multivariate regression reveals iron and myelin as independent contributors to all three types of contrast. The regression plots of univariate and multivariate linear regression analysis and their comparison are presented in Fig. 3. The simulated MR maps as functions of myelin and iron concentration and the original MR data (Fig. 4) allow an assessment of the quality of our linear regression approach. A summary of the regression coefficients and fraction of contrast that can be explained either by myelin or iron is listed in Table 1.

#### Calculation of element maps

The calculated iron and myelin maps are shown in Fig. 5. The subthalamic nucleus has higher iron concentration at the ventral–medial edge and higher myelin concentrations at the dorsal–lateral edge. These concentration gradients allow calculation of the elementary iron and myelin distributions from the MRI images. PIXE maps of iron, phosphorus and sulfur were measured to validate the calculated maps. A myelin map was inferred from the phosphorus and sulfur maps.

#### Discussion

For the first time, we have combined qualitative and quantitative techniques to investigate the combined contribution of iron and myelin

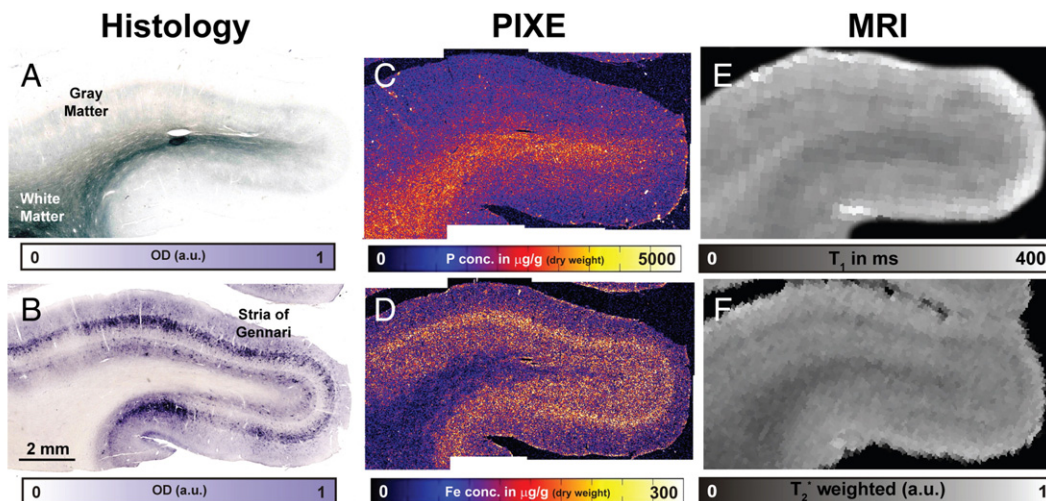


**Fig. 2.** Primary visual cortex containing the stria of Gennari (V1). (A–B) Histology. (A) Sudan-Black B stain showing lipids. (B) CRTL-1 (cartilage link protein), which is a vital part of the perineuronal nets, a specialized neuronal extracellular matrix structure found in the cortex, which has been shown to be associated with high-iron concentrations (immunohistochemistry). (C–D) PIXE-measurements. (C) Phosphorus map. (D) Iron map. (E–F) MRI. (E)  $T_1$  map. (F)  $T_2^*$  weighted image. The high concentration of iron in the stria of Gennari is clearly visible, as well as low concentration in white matter compared to cortical gray matter.



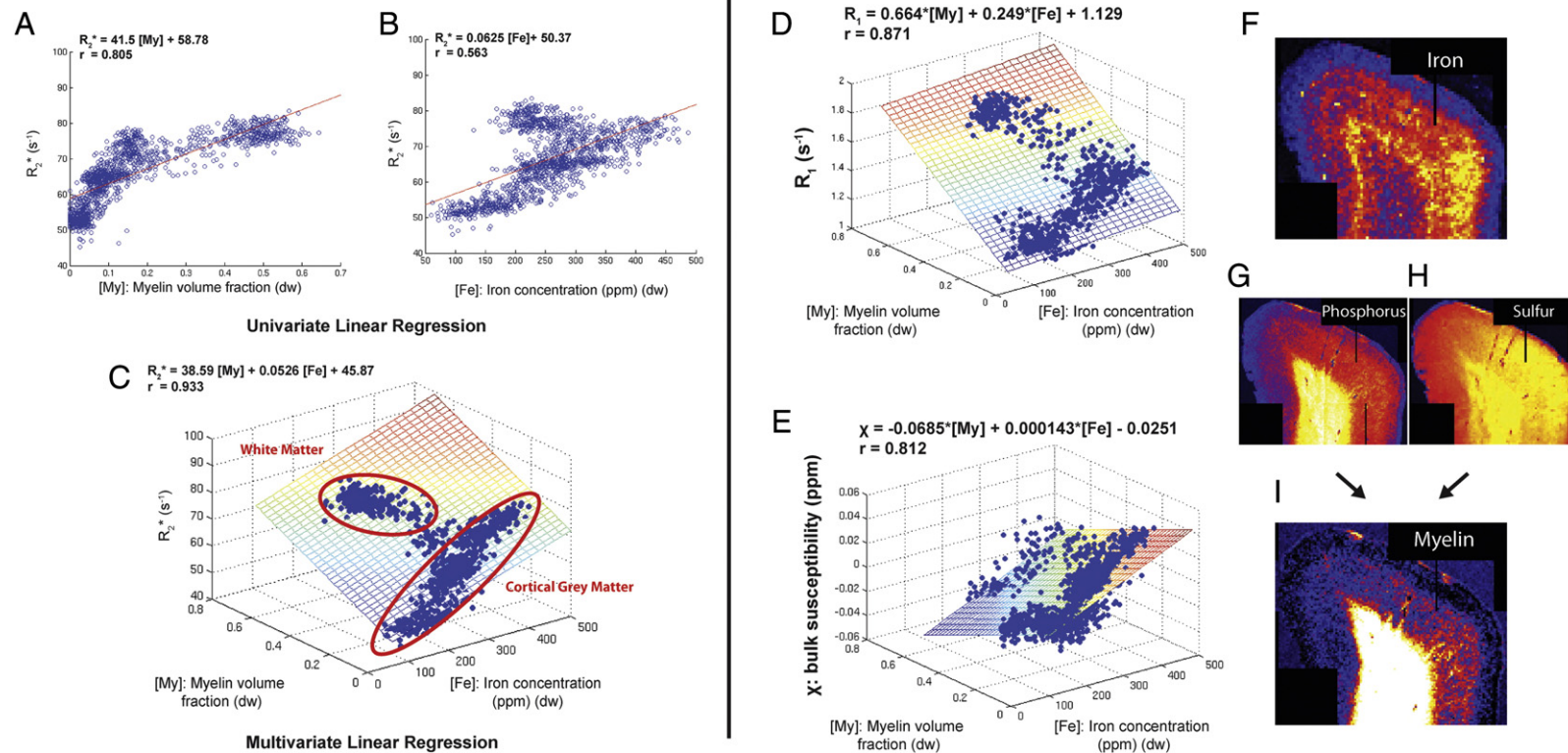


**Fig. 3.** Comparison of univariate and multivariate linear regression analysis – correlation of myelin volume fraction [My] and iron concentration [Fe] in dry tissue weight (dw) and  $R_2^*$  (7 T). Linear regression equation:  $R_2^* = \text{slope} * (\text{myelin volume fraction/iron concentration}) + \text{offset}$ .  $r =$  Pearson product-moment correlation coefficient. (A and B) Univariate linear regression: the straight line indicates the linear fit of  $R_2^*$  as a function of (A) myelin volume fraction and (B) iron concentration. (C) Multivariate linear regression: the plane indicates the linear fit with two variables. A good correlation between iron and myelin is clearly visible in the cortical areas. Furthermore  $R_2^*$  is larger in white matter, which corresponds to the dark appearing white matter in  $T_2^*$  maps. (D and E) Multivariate linear regression of  $T_1$  and QSM as a function of iron concentration [Fe] and myelin volume fraction [My] in dry tissue weight (dw) and  $R_2^*$  (7 T). (D) The linear regression of  $R_1$  shows a predominant role of myelin, but as well an impact of iron indicated by a small slope. (E) The regression analysis of QSM yields a negative slope for diamagnetic myelin and a positive slope for paramagnetic iron. (F–I) Quantitative maps in the primary motor cortex (M1): (F) PIXE iron map, (G) PIXE phosphorus map, (H) PIXE sulfur map, (I) Inferred myelin map calculated from Eq. (9).

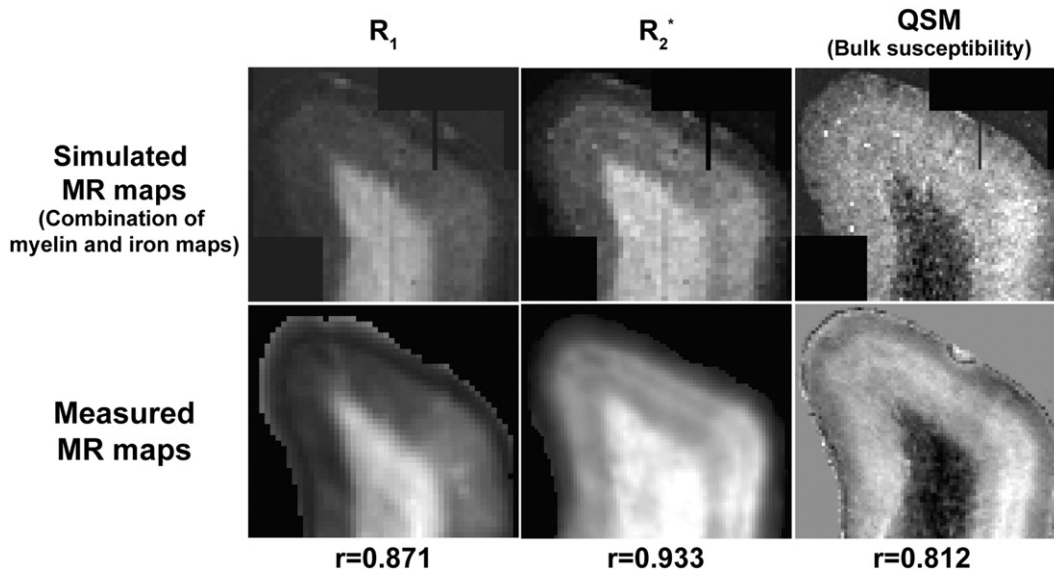


**Fig. 4.** Comparison of simulated and measured MR maps ( $R_1$ ,  $R_2^*$ , QSM).  $r$  = Pearson product-moment correlation coefficient. The cortical gray and white matter is clearly visible in all three sequences, although the cortex appears to be thicker in QSM.

as sources of MRI tissue contrast, for three standard image acquisition techniques. The quantification of myelin using the PIXE technique depends on some reasonable assumptions regarding the distribution of phosphorus and sulfur in brain tissue. The validity of these assumptions could be investigated in further research.

We have shown that both iron and myelin contribute in different proportions to contrast in maps of  $R_1$ ,  $R_2^*$  and quantitative magnetic susceptibility. We have validated previously proposed models which assumed a linear relationship between iron and myelin concentrations and the local Larmor frequency. Regressing the effects of myelin and iron jointly rather than separately yields much tighter correlations between their concentrations and the measured MR parameters (Figs. 3A–E). For example the correlation between  $R_2^*$  and iron shows a slope of  $0.0625 \pm 0.0017$  Hz/ppm. This measurement is in agreement with previous measurements of Yao et al. (2009) who predicted a slope of 0.0099 Hz/T/ppm dry weight, corresponding to 0.0693 Hz/ppm for 7 T. Nevertheless the Pearson's correlation coefficient of our data equals  $r = 0.77$  for iron- $R_2^*$  relationship. The combined correlation of iron and inferred myelin yields a much higher correlation coefficient of  $r = 0.93$  with a smaller slope for iron ( $a_{Fe} = 0.053 \pm 0.0011$  Hz/ppm) and a contribution for myelin ( $a_{My} = 38.59 \pm 0.5$  Hz / (myelin volume fraction)) (Fig. 3C and Table 1).

#### Histology/PIXE

The MBP stain shows a good overlap with the produced PIXE myelin map (Figs. 1A and 3I), which was obtained by subtraction of the non-myelin fraction in phosphorus maps aided by sulfur maps. Similarly,

the lipid stain shows a good correlation with the phosphorus map, which indicates that most phosphorus is bound to phospholipids (Figs. 2A and C).

The phosphorus map shows significant concentration variations within WM (Figs. 1C and 2C). This suggests that besides changes in myelin concentration due to fiber density variations (Fu et al., 2008), variations in lipid composition may also be responsible for the observed MRI contrast variations in white matter (Norton and Cammer, 1984; Veloso et al., 2011).

The PIXE iron maps and the histological sections with Perls' iron stain show patchiness in white matter (Figs. 1B and D), consistent with that previously observed using the Perls' stain (Connor and Menzies, 1995; Connor et al., 1990). These earlier results are questionable due to the well-known difficulties in obtaining robust white matter staining (Todorich et al., 2009). This white matter patchiness has also been detected in microscopic MRI at high field strength, and it has already been suggested that this structure may be related to iron distribution (Li et al., 2010). Some iron is stored in oligodendrocytes. These iron-positive cells in white matter are associated with blood vessels and are found primarily in myelinogenic foci, the source of myelination in white matter, which leads to the view that this oligodendrocytic iron plays a vital role in the onset of myelination (Connor and Menzies, 1996). Although the iron map and  $T_2^*$  weighted image showed patches of the same size and shape, these patches were too small to enable sufficiently accurate registration for investigation of the correlation between iron content and  $T_2^*$ .

Basically, the most obvious differences in iron distributions within white and gray matter are that cortical areas show a relatively

**Table 1**  
Results of the multivariate linear regression analysis for  $R_1$ ,  $R_2^*$  and QSM.

	Iron Regression slopes $R_1, R_2^*$ : (in kg/mg (dw) $s^{-1}$ ) (in kg/mg (dw) ppm)	Contrast portion		Myelin Regression slopes $R_1, R_2^*$ : (in (MVF) $^{-1} s^{-1}$ ) QSM: (in (MVF) $^{-1}$ ppm)	Contrast portion		Offset
		GM	WM		GM	WM	
$R_1$	$0.000223 \pm 0.000034$	0.36	0.10	$1.066 \pm 0.016$	0.64	0.90	$1.132 \pm 0.009$
$R_2^*$	$0.0526 \pm 0.0011$	0.81	0.44	$38.59 \pm 0.50$	0.19	0.56	$45.86 \pm 0.29$
QSM	$0.000143 \pm 0.000004$	0.67	0.28	$-0.069 \pm 0.002$	0.33	0.72	$-0.025 \pm 0.001$

The regression slopes are given for iron and myelin in mean  $\pm$  standard deviation.

The p-values are below 0.001 in all analysis.

The portion of contrast caused by iron or myelin is given and separated for gray matter (GM) and white matter (WM) in the motor-/somatosensory cortex.



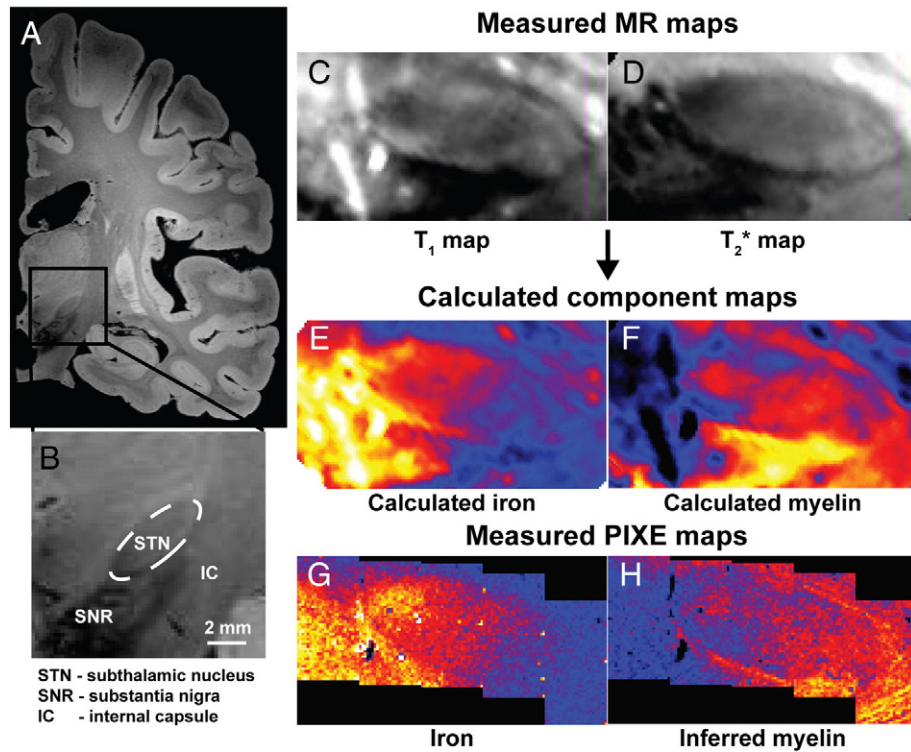


**Fig. 5.** Calculating element maps from MR-images (subthalamic nucleus–basal ganglia). (A)  $T_2^*$  weighted image of the right hemisphere of a human post-mortem brain. (B) The magnification shows the location of the lens-shaped subthalamic nucleus (STN) adjacent to the iron-rich substantia nigra (SN), appearing hypointense on the  $T_2^*$  weighted image (coronal view). (C)  $T_1$  map and (D)  $T_2^*$  map of the STN (rotated maps). (E and F) The maps were calculated from Eq. 10 and Eq. 11 using the coefficients associated with iron and myelin  $a_{Fe}$ ,  $b_{Fe}$ ,  $a_{My}$ , and  $b_{My}$  and the offset  $a_{off}$  and  $b_{off}$  obtained from the multivariate linear regression analysis (Methods). (E) Calculated iron map: The iron concentration increases at the ventral–medial cap. The bright adjacent iron-rich area can be attributed to the SN, which was shown to contain a high iron concentration. (F) The calculated myelin map shows a rim around the nucleus and myelinated fibers penetrate along the long axis of the nucleus from the lateral edge. (G) Measured iron and (H) inferred myelin maps show a similar distribution compared to the calculated maps, although the heavy myelinated fibers of the internal capsule at the dorsal–lateral side are not clearly visible in the calculated myelin map.

homogeneous laminar distribution of iron, whereas iron in white matter shows a “clustered” structure. The data thus support the hypothesis of Duyn’s laboratory of a strong association between iron and cortical myelin, which is not found in white matter myelin (Fukunaga et al., 2010).

It is important to note that during the preparation of the samples any water-soluble iron compound was likely to be washed out. Free iron, which is not stored in iron-related proteins such as ferritin or transferrin, constitutes the labile iron pool. It comprises only a minor fraction of the total iron content (<5%) (Kakhlon and Cabantchik, 2002). Similarly, brain tissue fixation clearly washes out mobile phosphorus-containing molecules, such as energy metabolites and inorganic phosphates, such that the remaining phosphorus is found in phospholipids. This circumstance enables the link that we have explored between phosphorus content and myelin content. Some further loss of phosphorus during fixation and later slice preparation is possible. Quantitative assays of brain tissue phosphorus are rare in the literature. Tohno et al. (2011) obtained similar concentrations of about 5 mg/g in the myelinated optic nerve fibers, while our data suggest a maximum of about 6 mg/g in white matter. Further careful quantitative studies in cadaver brain and in vivo with MR spectroscopic techniques will help to address this issue.

## $R_1$

The measured  $T_1$  for postmortem samples is shorter than that for in vivo. Formalin fixation is known to shorten  $T_1$  in the brain considerably (Tovi and Ericsson, 1992), but has little effect on the quality of MRI (Nagara et al., 1987), as long as the sequence parameters are appropriately chosen. Thus a histogram of  $T_1$  values in cadaver brain has a similar appearance with a narrow peak at shorter  $T_1$  corresponding to

white matter and a broader peak that includes the cortical gray matter and deep brain structures (Oros-Peusquens et al., 2012). We found differences of  $T_1$  between high and low cortical myelin content areas of 15–25%, as found by previous studies (Bock et al., 2009). The linear model of Rooney et al. (2007) is confirmed by our results, with nearly the same iron contribution ( $0.047(\pm 0.012) \text{ s}^{-1}/\text{mM}$  or  $1.175 \text{ s}^{-1}/\text{mg/g}$  in wet weight, which corresponds to  $0.235 \text{ s}^{-1}/\text{mg/g}$  dry weight) compared to our results of  $0.223 (\pm 0.034) \text{ s}^{-1}/\text{mg/g}$  in dry weight (roughly 5:1 fresh to dry weight ratio) (MacKay et al., 2006) (Table 1 and Fig. 3D). Furthermore our experiments give a slope of  $R_1$  vs. a myelin volume fraction of  $1.07 (\pm 0.01) \text{ s}^{-1}/\text{MVf}$  in dry weight compared to  $1.8 (\pm 0.1) \text{ s}^{-1}/\text{MVf}$  for the “macromolecular” fraction measured in wet weight. The regression analysis yields a much higher impact of myelin compared to iron, which is also seen in the simulated MR maps (Fig. 4). We found that iron has an average contribution of 10% in white matter and 36% in gray matter (Table 1).

## Deferoxamine

The loss of cortical contrast in  $R_1$  maps after iron extraction is easily visible in the cortex (Fig. 6B) compared to the untreated sample (Fig. 6A). Some remaining intracortical contrast in the treated sample is visible, which can be attributed to the presence of myelin lipids. The profiles taken perpendicular to the surface show a strong difference in contrast by  $0.07 \text{ s}^{-1}$  in white matter beneath the cortical surface and up to  $0.14 \text{ s}^{-1}$  intracortically, where myelination and iron concentration are highest (Fig. 6E). The average intracortical difference of the profiles, the area between both curves, amounts to  $0.102 \text{ s}^{-1}$ . This loss corresponding to an intracortical reduction of  $R_1$  by roughly 30% is in agreement with our simulation that iron contributes 36% of the cortical contrast and myelin the remaining 64% (Table 1), given an offset of

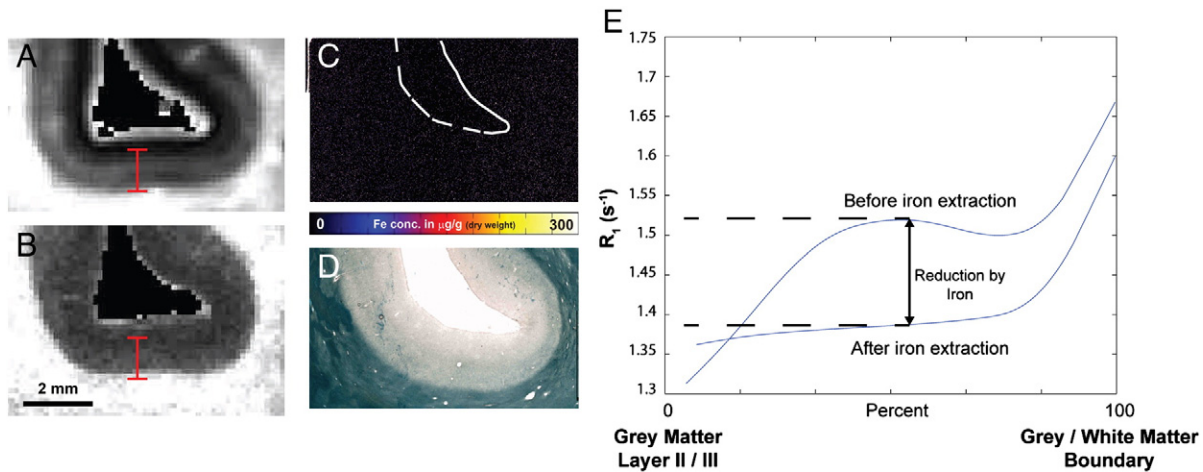


**Fig. 6.** Removal of iron — effect of deferoxamine (sulcus of motor/somatosensory cortex). (A)  $R_1$ -map before and (B) after iron-extraction. (C) PIXE-map of iron showing almost no iron signal, the bright strip in the upper left corner belongs to the metallic frame of the sample, the dashed lines indicate the location of the pial surface. (D) Sudan-black lipid stain, the lipid distribution shows the same cortical structures after the iron-extraction, the lipids largely remain in the sample and do not seem to be heavily affected by the iron-extraction process. (E) Profiles taken perpendicular to white matter/gray matter boundary showing a reduction of  $R_1$  rate, in particular in cortical regions of high iron concentrations.

$1.129 (\pm 0.009) \text{ s}^{-1}$  in  $R_1$  maps. The profiles also show differences in an adjacent white matter of about  $0.07 \text{ s}^{-1}$ , which can be explained by the loss of iron. Use of the PIXE technique demonstrated that the iron extraction was successful (Fig. 6C). The residual mean iron concentration is  $16.1 (\pm 12.4) \text{ mg/g}$  (dry weight), thus a large fraction of the metal is extracted ( $>90\%$ ). Furthermore the lipid stain after iron extraction indicates that the distribution of myelin lipids is not heavily affected by the procedure of the extraction process (Fig. 6D), although some damage to remaining tissue components by the chemical treatment cannot be excluded.

## $R_2^*$

The MR images, characterized by cortical lamination and some heterogeneity in white matter, show lower  $R_2^*$  rates in white matter compared to gray matter, although the differences are small. However, the fastest relaxation is found within the cortex, as also seen in the simulated  $R_2^*$  maps (Fig. 4). The multivariate linear regression yields a predominant role of iron as a source of  $R_2^*$  contrast. Even in white matter, with its high myelin concentration, iron still explains roughly half of the contrast (Table 1).

Although some of the observed  $R_2^*$  contrast in white matter appears to show a fascicle-specific dependence, the precise origin of this effect is not yet clear. There are several potential factors determining  $R_2^*$  that can vary between fiber bundles, including iron content (Haacke et al., 2005), myelin content and structure, and the fiber direction relative to the main magnetic field (Chappell et al., 2004; Cherubini et al., 2009; Cohen-Adad et al., 2012).

To include the observable dependency on myelin orientation, this model has been recently extended (Schweser et al., 2012).

## QSM

The most striking characteristic of QSM maps is the apparent thicker cortex compared to histology (Fig. 3). This is caused by the paramagnetic iron rim at the surface of the white matter suppressing the dark-appearing diamagnetic myelin. The measured regression coefficients for iron are in line with previous determined values: the combined study of iron in gray and white matter yields  $0.000143 \pm 0.000004 \text{ ppm per mg/kg dry weight}$  (corresponds to approximately  $0.000715 \text{ ppm per mg/kg wet weight}$ ), which is in the range of  $0.00089 \text{ (GM)}$  and  $0.00055 \text{ (WM)}$  (ppm per mg/kg wet weight) given in Langkammer et al. (2012). It is known that iron is about 30 times more abundant than other transition elements in the brain, which means that their paramagnetic effects can be neglected.

Despite good visual agreement between the simulated and measured QSM maps, the Pearson's correlation coefficient in the regression analysis is smaller than that found with the other maps studied (Fig. 3E and Fig. 4). This may be explained by the fact that magnetic susceptibility is a tensor quantity. Since the orientation dependency of the susceptibility of myelinated fibers cannot be measured with the PIXE element maps, it is obvious that measured mean bulk susceptibility may vary independently from myelin concentration. Due to the anisotropy of the myelin sheath, QSM maps show contrast differences in white matter regions with varying fiber direction (Wharton and Bowtell, 2012).

## Splitting MR images into iron and myelin

The inverse approach, calculating from MR images the components that mainly determine MR tissue contrast, shows comparably good results. While the iron map almost exactly matches the measured PIXE iron map, the myelin map differs in some regions neighboring the subthalamic nucleus, such as the internal capsule, and heavily myelinated ascending and descending axons (Fig. 5). The reason could be the fiber direction dependency in  $T_2^*$  maps, in particular visible in fiber bundles with a preferential direction.

The next step, regarding the experiments and the potential implications for imaging neuroscience, cognitive neuroscience, neuroanatomy, neurology and psychiatry, is going from ex- to in-vivo. An approach to compare ex-vivo and in-vivo could be done in mouse models, enabling the comparison of in-vivo and ex-vivo MR scans and of PIXE measurements of fixed and unfixed brain tissue.

From our studies, we conclude that myelin is the dominant source of MRI contrast in  $T_1$  maps and iron the dominant source of contrast in  $T_2^*$  maps. We have shown that the quantities  $R_1$ ,  $R_2^*$  and  $\chi$  are all linearly related to iron and myelin concentrations. This provides some support for the use of MRI sequences that measure these quantitative parameters in clinical imaging, for instance of patients with disorders related to brain iron deposits or loss of myelin such as Parkinson disease (Morawski et al., 2005) and multiple sclerosis (Schmierer et al., 2010). Quantitative susceptibility mapping has the potential to become a biomarker for abnormal cortical iron distribution in clinical applications due to its easy visibility. Regarding white matter, and in particular myelin,  $T_1$  mapping is an appropriate method for mapping myelin concentration as it is largely unaffected by the direction of myelinated fibers seen in  $R_2^*$  and QSM, and its value depends much more strongly on myelin concentration than on iron concentration. Combined acquisition of  $T_1$  and  $T_2^*$  maps, together with maps of the magnetic susceptibility

tensor and fiber orientation, has the potential to generate in vivo quantitative maps of myelin and iron densities.

Supplementary data to this article can be found online at <http://dx.doi.org/10.1016/j.neuroimage.2014.02.026>.

## Acknowledgments

The authors thank Prof. Dr. Jürgen Haase and Dr. Jürgen Vogt from the faculty of Physics And Geosciences at the University of Leipzig for their support and for providing access to the Leipzig ion beam laboratory (LIPSION), and Marcel Weiss, Gabriele Lohmann and Pierre-Louis Bazin at the Max Planck Institute for Human Cognitive and Brain Sciences for support and valuable discussion.

This work was supported by the COST Action BM1001 “Brain Extracellular Matrix in Health and Disease”, the Alzheimer Forschungsinitiative e.V. (AFI #11861), the European Union and the Free State of Saxony (grant number EU-ESF 100154907), the German Research Foundation (DFG) MO 2249/2-1 within the PP 1608 and the GRK 1097 “INTERNEURO” Project P8 to M. M.

## Competing financial interests

The authors declare no competing financial interests.

## References

- Abdul-Rahman, H.S., Gdeisat, M.A., Burton, D.R., Lalor, M.J., Lilley, F., Moore, C.J., 2007. Fast and robust three-dimensional best path phase unwrapping algorithm. *Appl. Optics* 46 (26), 6623–6635.
- Barbier, E.L., Marrett, S., Danek, A., Vortmeyer, A., van Gelderen, P., Duyn, J., Bandettini, P., Grafman, J., Koretsky, A.P., 2002. Imaging cortical anatomy by high-resolution MR at 3.0 T: detection of the stripe of Gennari in visual area 17. *Magn. Reson. Med.* 48 (4), 735–738.
- Bender, B., Klose, U., 2010. The in vivo influence of white matter fiber orientation towards  $B_0$  on  $T_2^*$  in the human brain. *NMR Biomed.* 23 (9), 1071–1076.
- Bock, N.A., Kocharyan, A., Liu, J.V., Silva, A.C., 2009. Visualizing the entire cortical myelination pattern in marmosets with magnetic resonance imaging. *J. Neurosci. Methods* 185 (1), 15–22.
- Bookstein, F.L., 1989. Principal warps: thin-plate splines and the decomposition of deformations. *IEEE Trans. Pattern Anal.* 11 (6), 567–585.
- Bot, J., Blezer, E., Kamphorst, W., Nijeholt, G., Ader, H.J., Castellijn, J.A., Nicolay, K., Bergers, E., Ravid, R., Polman, C., Barkhof, F., 2004. The spinal cord in multiple sclerosis: relationship of high-spatial-resolution quantitative MR imaging findings to histopathologic results. *Radiology* 233 (2), 531–540.
- Buchli, R., Duc, C., Martin, E., Boesiger, P., 1994. Assessment of absolute metabolite concentrations in human tissue by 31P MRS in vivo. Part I: cerebrum, cerebellum, cerebral gray and white matter. *Magn. Reson. Med.* 32 (4), 447–452.
- Butz, T., Meinecke, C., Morawski, M., Reinert, T., Schwertner, M., Spemann, D., Vogt, J., 2005. Morphological and elemental characterization with the high-energy ion-nanoprobe LIPSION. *Appl. Surf. Sci.* 252 (1), 43–48.
- Chappell, K.E., Robson, M.D., Stonebridge-Foster, A., Glover, A., Allsop, J.M., Williams, A.D., Herlihy, A.H., Moss, J., Gishen, P., Bydder, G.M., 2004. Magic angle effects in MR neurography. *AJNR Am. J. Neuroradiol.* 25 (3), 431–440.
- Chavhan, G.B., Babyn, P.S., Thomas, B., Shroff, M.M., Haacke, E.M., 2009. Principles, techniques, and applications of  $T_2^*$ -based MR imaging and its special applications. *Radiographics* 29 (5), 1433–1449.
- Cherubini, A., Péran, P., Hagberg, G.E., Varsi, A.E., Luccichenti, G., Caltagirone, C., Sabatini, U., Spalletta, G., 2009. Characterization of white matter fiber bundles with  $T_2^*$  relaxometry and diffusion tensor imaging. *Magn. Reson. Med.* 61 (5), 1066–1072.
- Clark, V.P., Courchesne, E., Grafe, M., 1991. In vivo myeloarchitectonic analysis of human striate and extrastriate cortex using magnetic resonance imaging. *Cereb. Cortex* 2 (5), 417–424.
- Cohen-Adad, J., Polimeni, J.R., Helmer, K.G., Benner, T., McNab, J.A., Wald, L.L., Rosen, B.R., Mainiero, C., 2012.  $T_2^*$  mapping and  $B_0$  orientation-dependence at 7 T reveal cyto- and myeloarchitecture organization of the human cortex. *NeuroImage* 60 (2), 1006–1014.
- Connor, J.R., Menzies, S.L., 1995. Cellular management of iron in the brain. *J. Neurol. Sci.* 134 (Suppl.), 33–44.
- Connor, J.R., Menzies, S.L., 1996. Relationship of iron to oligodendrocytes and myelination. *GLIA* 17 (2), 83–93.
- Connor, J.R., Menzies, S.L., St Martin, S.M., Mufson, E.J., 1990. Cellular distribution of transferrin, ferritin, and iron in normal and aged human brains. *J. Neurosci. Res.* 27 (4), 595–611.
- Doolittle, L.R., 1985. Algorithms for the rapid simulation of Rutherford backscattering spectra. *Nucl. Instr. Methods B* 9 (3), 344–351.
- Drayer, B., Burger, P., Darwin, R., Riederer, S., Herfkens, R., Johnson, G.A., 1986. MRI of brain iron. *AJ. Am. J. Roentgenol.* 147 (1), 103–110.
- Duyn, J.H., 2010. Study of brain anatomy with high-field MRI: recent progress. *Magn. Reson. Imaging* 28 (8), 1210–1215.
- Duyn, J.H., van Gelderen, P., Li, T.-Q., de Zwart, J.A., Koretsky, A.P., Fukunaga, M., 2007. High-field MRI of brain cortical substructure based on signal phase. *Proc. Natl. Acad. Sci. U. S. A.* 104 (28), 11796–11801.
- Eickhoff, S., Walters, N.B., Schleicher, A., Kril, J., Egan, G.F., Zilles, K., Watson, J.D.G., Amunts, K., 2005. High-resolution MRI reflects myeloarchitecture and cytoarchitecture of human cerebral cortex. *Hum. Brain Mapp.* 24 (3), 206–215.
- Fatterpekar, G.M., Naidich, T.P., Delman, B.N., Aguinaldo, J.G., Gultekin, S.H., Sherwood, C.C., Hof, P.R., Drayer, B.P., Fayad, Z.A., 2002. Cytoarchitecture of the human cerebral cortex: MR microscopy of excised specimens at 9.4 Tesla. *Am. J. Neuroradiol.* 23 (8), 1313–1321.
- Fu, Y., Huff, T., Wang, H., Cheng, J., Wang, H., 2008. Ex vivo and in vivo imaging of myelin fibers in mouse brain by coherent anti-Stokes Raman scattering microscopy. *Opt. Express* 16 (24), 19396–19409.
- Fukunaga, M., Li, T.-Q., van Gelderen, P., de Zwart, J.A., Shmueli, K., Yao, B., Lee, J., Maric, D., Aronova, M.A., Zhang, G., Leapman, R.D., Schenck, J.F., Merkle, H., Duyn, J.H., 2010. Layer-specific variation of iron content in cerebral cortex as a source of MRI contrast. *Proc. Natl. Acad. Sci. U. S. A.* 107 (8), 3834–3839.
- Gelman, N., Ewing, J.R., Gorell, J.M., Spickler, E.M., Solomon, E.G., 2001. Interregional variation of longitudinal relaxation rates in human brain at 3.0 T: relation to estimated iron and water contents. *Magn. Reson. Med.* 45 (1), 71–79.
- Geyer, S., Weiss, M., Reimann, K., Lohmann, G., Turner, R., 2011. Microstructural parcellation of the human cerebral cortex – from Brodmann's post-mortem map to in vivo mapping with high-field magnetic resonance imaging. *Front. Hum. Neurosci.* 5, 19. <http://dx.doi.org/10.3389/fnhum.2011.00019>.
- Glasser, M.F., Van Essen, D.C., 2011. Mapping human cortical areas in vivo based on myelin content as revealed by T1- and T2-weighted MRI. *J. Neurosci.* 31 (32), 11597–11616.
- Gossuin, Y., Roch, A., Muller, R.N., Gillis, P., 2000. Relaxation induced by ferritin and ferritin-like magnetic particles: the role of proton exchange. *Magn. Reson. Med.* 43 (2), 237–243.
- Haacke, E.M., Cheng, N.Y.C., House, M.J., Liu, Q., Neelavalli, J., Ogg, R.J., Khan, A., Ayaz, M., Kirsch, W., Obenaus, A., 2005. Imaging iron stores in the brain using magnetic resonance imaging. *Magn. Reson. Imaging* 23 (1), 1–25.
- Hallgren, B., Sourander, P., 1958. The effect of age on the non-haemin iron in the human brain. *J. Neurochem.* 3 (1), 41–51.
- Haraux, G., Ishiyama, N., Hill, C.M.D., Bates, I.R., Libich, D.S., Farès, C., 2004. Myelin basic protein-diverse conformational states of an intrinsically unstructured protein and its roles in myelin assembly and multiple sclerosis. *Micron* 35 (7), 503–542.
- Jahn, O., Tenzer, S., Werner, H.B., 2009. Myelin proteomics: molecular anatomy of an insulating sheath. *Mol. Neurobiol.* 40 (1), 55–72.
- Kakhlon, O., Cabantchik, Z.I., 2002. The labile iron pool: characterization, measurement, and participation in cellular processes. *Free Radic. Biol. Med.* 33 (8), 1037–1046.
- Koenig, S.H., 1991. Cholesterol of myelin is the determinant of gray-white contrast in MRI of brain. *Magn. Reson. Med.* 20 (2), 285–291.
- Koenig, S.H., Brown, R.D., Spiller, M., Lundbom, N., 1990. Relaxometry of brain: why white matter appears bright in MRI. *Magn. Reson. Med.* 14 (3), 482–495.
- Kucharczyk, W., Macdonald, P.M., Stanisz, G.J., Henkelman, R.M., 1994. Relaxivity and magnetization transfer of white matter lipids at MR imaging: importance of cerebroside and pH. *Radiology* 192 (2), 521–529.
- Labadie, C., Lee, J.-H., Rooney, W.D., Jarchow, S., Aubert-Frécon, M., Springer, C.S., Möller, H.E., 2014. Myelin water mapping by spatially regularized longitudinal relaxographic imaging at high magnetic fields. *Magn. Reson. Med.* 71 (1), 375–387.
- Langkammer, C., Krebs, N., Goessler, W., Scheurer, E., Yen, K., Fazekas, F., Ropele, S., 2011. Susceptibility induced gray-white matter MRI contrast in the human brain. *NeuroImage* 59 (2), 1413–1419.
- Langkammer, C., Schweser, F., Krebs, N., Deistung, A., Goessler, W., Scheurer, E., Sommer, K., Reishofer, G., Yen, K., Fazekas, F., Ropele, S., Reichenbach, J.R., 2012. Quantitative susceptibility mapping (QSM) as a means to measure brain iron? A post mortem validation study. *NeuroImage* 62 (3), 1593–1599.
- Laule, C., Vavasour, I.M., Kolind, S.H., Li, D.K.B., Traboulsee, T.L., Moore, G.R.W., MacKay, A.L., 2007. Magnetic resonance imaging of myelin. *Neurotherapeutics* 4 (3), 460–484.
- Laule, C., Kozlowski, P., Leung, E., Li, D.K.B., Mackay, A.L., Moore, G.R.W., 2008. Myelin water imaging of multiple sclerosis at 7 T: correlations with histopathology. *NeuroImage* 40 (4), 1575–1580.
- Li, T.-Q., Yao, B., van Gelderen, P., Merkle, H., Dodd, S., Talagala, L., Koretsky, A.P., Duyn, J., 2009. Characterization of  $T_2^*$  heterogeneity in human brain white matter. *Magn. Reson. Med.* 62 (6), 1652–1657.
- Li, T.-Q., Fukunaga, M., Shmueli, K., Dodd, S., Duyn, J.H., 2010. Patch structure in white matter detected by microscopic MRI at high field strength. *Proc. Int. Soc. Magn. Reson. Med.* 18, 2304.
- Li, W., Wu, B., Liu, C., 2011. Quantitative susceptibility mapping of human brain reflects spatial variation in tissue composition. *NeuroImage* 55 (4), 1645–1656.
- MacKay, A., Laule, C., Vavasour, I., Bjarnason, T., Kolind, S., Mädler, B., 2006. Insights into brain microstructure from the T2 distribution. *Magn. Reson. Imaging* 24 (4), 515–525.
- Marques, J.P., et al., 2010. MP2RAGE, a self bias-field corrected sequence for improved segmentation and T1-mapping at high field. *NeuroImage* 49 (2), 1271–1281.
- Morawski, M., Meinecke, C., Reinert, T., Dörfel, A.C., Riederer, P., Arendt, T., Butz, T., 2005. Determination of trace elements in the human substantia nigra. *Nucl. Instr. Methods B* 231 (1–4), 224–228.
- Mottershead, J.P., Schmierer, K., Clemence, M., Thornton, J.S., Scaravilli, F., Barker, G.J., Tofts, P.S., Newcombe, J., Cuzner, M.L., Ordridge, R.J., McDonald, W.I., Miller, D.H., 2003. High field MRI correlates of myelin content and axonal density in multiple sclerosis – a post-mortem study of the spinal cord. *J. Neurol.* 250 (11), 1293–1301.



- Nagara, H., Inoue, T., Koga, T., Kitaguchi, T., Tateishi, J., Goto, I., 1987. Formalin fixed brains are useful for magnetic resonance imaging (MRI) study. *J. Neurol. Sci.* 81 (1), 67–77.
- Ng, D.P., Deber, C.M., 2010. Modulation of the oligomerization of myelin proteolipid protein by transmembrane helix interaction motifs. *Biochemistry* 49 (32), 6896–6902.
- Norton, W.T., Autilio, L.A., 1966. The lipid composition of purified bovine brain myelin. *J. Neurochem.* 13 (4), 213–222.
- Norton, W., Cammer, W., 1984. Isolation and characterization of myelin. In: Morell, P. (Ed.), *Myelin*. Plenum Press, New York, pp. 147–195.
- O'Brien, J.S., 1965. Stability of the myelin membrane. *Science* 147 (3662), 1099–1107.
- O'Brien, J., Sampson, E., 1965. Lipid composition of the normal human brain: gray matter, white matter, and myelin. *J. Lipid Res.* 15 (3), 537–544.
- Ogg, R.J., Steen, R.G., 1998. Age-related changes in brain T1 are correlated with iron concentration. *Magn. Reson. Med.* 40 (5), 749–753.
- Ordidge, R.J., Gorell, J.M., Deniau, J.C., Knight, R.A., Helpert, J.A., 1994. Assessment of relative brain iron concentrations using T2-weighted and T2\*-weighted MRI at 3 Tesla. *Magn. Reson. Med.* 32 (3), 335–341.
- Oros-Peusquens, A.-M., Matusch, A., Lindermeier, J., Becker, J.S., Shah, N.J., 2012. Changes in MR contrast after fixation: insight from M0, R2\*, phase and element imaging by LA-ICP-MS. *Proc. Int. Soc. Magn. Reson. Med.* 20, 383.
- Reichenbach, J.R., 2012. The future of susceptibility contrast for assessment of anatomy and function. *NeuroImage* 62 (2), 1311–1315.
- Reinert, T., Andrea, T., Barapatre, N., Hohlweg, M., Koal, T., Larisch, W., Reinert, A., Spemann, D., Vogt, J., Werner, R., Butz, T., 2011. Biomedical research at LIPSION – present state and future developments. *Nucl. Instr. Methods B* 269 (20), 2254–2259.
- Rooney, W.D., Johnson, G., Li, X., Cohen, E.R., Kim, S.-G., Ugurbil, K., Springer, C.S., 2007. Magnetic field and tissue dependencies of human brain longitudinal  $^1\text{H}_2\text{O}$  relaxation in vivo. *Magn. Reson. Med.* 57 (2), 308–318.
- Ryan, C.G., 2001. Developments in dynamic analysis for quantitative PIXE true elemental imaging. *Nucl. Instr. Methods B* 181 (1–4), 170–179.
- Schäfer, A., Forstmann, B.U., Neumann, J., Wharton, S.J., Mietke, A., Bowtell, R., Turner, R., 2012. Direct visualization of the subthalamic nucleus and its iron distribution using high-resolution susceptibility mapping. *Hum. Brain Mapp.* 33 (12), 2831–2842.
- Schenck, J.F., Zimmerman, E.A., 2004. High-field magnetic resonance imaging of brain iron: birth of a biomarker? *NMR Biomed.* 17 (7), 433–445.
- Schmierer, K., Scaravilli, F., Altmann, D.R., Barker, G.J., Miller, D.H., 2004. Magnetization transfer ratio and myelin in postmortem multiple sclerosis brain. *Ann. Neurol.* 56 (3), 407–415.
- Schmierer, K., Parkes, H.G., So, P.-W., An, S.F., Brandner, S., Ordridge, R.J., Yousry, T.A., Miller, D.H., 2010. High field (9.4 Tesla) magnetic resonance imaging of cortical grey matter lesions in multiple sclerosis. *Brain* 133 (Pt 3), 858–867.
- Schweser, F., Deistung, A., Lehr, B.W., Sommer, K., Reichenbach, J.R., 2011. SEMI-TWInS: simultaneous extraction of myelin and iron using a T2\*-weighted imaging sequence. *Proc. Int. Soc. Magn. Reson. Med.* 19, 120.
- Schweser, F., Deistung, A., Sommer, K., Reichenbach, J.R., 2012. Disentangling contributions from iron and myelin architecture to brain tissue magnetic susceptibility by using quantitative susceptibility mapping (QSM). *Proc. Int. Soc. Magn. Reson. Med.* 20, 409.
- Sigalovsky, I., Fischl, B., Melcher, J., 2006. Mapping an intrinsic MR property of gray matter in auditory cortex of living humans: a possible marker for primary cortex and hemispheric differences. *NeuroImage* 32 (4), 1524–1537.
- Steen, R.G., Reddick, W.E., Ogg, R.J., 2000. More than meets the eye: significant regional heterogeneity in human cortical T1. *Magn. Reson. Imaging* 18 (4), 361–368.
- Todorich, B., Pasquini, J., Garcia, C., Paez, P., 2009. Oligodendrocytes and myelination: the role of iron. *GLIA* 57 (5), 467–478.
- Tohno, S., Ishizaki, T., Shida, Y., Tohno, Y., Minami, T., Mahakkanukrauh, P., 2011. Element distribution in visual system, the optic chiasma, lateral geniculate body, and superior colliculus. *Biol. Trace Elem. Res.* 142 (3), 335–349.
- Tovi, M., Ericsson, A., 1992. Measurements of T1 and T2 over time in formalin-fixed human whole-brain specimens. *Acta Radiol.* 33 (5), 400–404.
- Trampel, R., Ott, D.V.M., Turner, R., 2011. Do the congenitally blind have a stria of Gennari? First intracortical insights in vivo. *Cereb. Cortex* 21 (9), 2075–2081.
- Veloso, A., Astigarraga, E., Barreda-Gómez, G., Manuel, I., Ferrer, I., Giralt, M.T., Ochoa, B., Fresnedo, O., Rodríguez-Puertas, R., Fernández, J.A., 2011. Anatomical distribution of lipids in human brain cortex by imaging mass spectrometry. *J. Am. Soc. Mass Spectrom.* 22 (2), 329–338.
- Vymazal, J., Hajek, M., Patronas, N., 1995. The quantitative relation between T1-weighted and T2-weighted MRI of normal gray matter and iron concentration. *J. Magn. Reson. Imaging* 5 (5), 556–560.
- Walters, N.B., Eickhoff, S.B., Schleicher, A., Zilles, K., Amunts, K., Egan, G.F., Watson, J.D.G., 2007. Observer-independent analysis of high-resolution MR images of the human cerebral cortex: in vivo delineation of cortical areas. *Hum. Brain Mapp.* 28 (1), 1–8.
- Wharton, S., Bowtell, R., 2012. Fiber orientation-dependent white matter contrast in gradient echo MRI. *Proc. Natl. Acad. Sci. U. S. A.* 109 (45), 18559–18564.
- Wharton, S., Schäfer, A., Bowtell, R., 2010. Susceptibility mapping in the human brain using threshold-based k-space division. *Magn. Reson. Med.* 63 (5), 1292–1304.
- Yan, S.-Q., Sun, J.-Z., Yan, Y.-Q., Wang, H., Lou, M., 2012. Evaluation of brain iron content based on magnetic resonance imaging (MRI): comparison among phase value, R2\* and magnitude signal intensity. *PLoS ONE* 7 (2), 1–6.
- Yao, B., Li, T.-Q., van Gelderen, P., Shmueli, K., de Zwart, J.A., Duyn, J.H., 2009. Susceptibility contrast in high field MRI of human brain as a function of tissue iron content. *NeuroImage* 44 (4), 1259–1266.